Rare Metal Materials and Engineering
Volume 50, Issue 10, October 2021
Available online at www.rmme.ac.cn

Science Press

Cite this article as: Ren Huilan, Shen Haiting, Ning Jianguo. Deformation Failure of Regular Porous Titanium with Different Porosities[J]. Rare Metal Materials and Engineering, 2021, 50(10): 3495-3503.

ARTICLE

Deformation Failure of Regular Porous Titanium with Different Porosities

Ren Huilan, Shen Haiting, Ning Jianguo

State Key Laboratory of Explosion Science and Technology, Beijing Institute of Technology, Beijing 100081, China

Abstract: Regular porous titanium specimens with different porosities was fabricated to investigate the overall and local failure characteristics of porous metals. Dynamic compression tests were implemented using the split Hopkinson pressure bar system at the strain rates from 600 s^{-1} to 2100 s^{-1}. Results show that the specimens with different porosities exhibit two typical deformation modes: compression deformation mode and connected fracture mode. The compression deformation mode mainly occurs in the specimens with low porosity, and the characteristic is that the cell walls of outer surface of the specimen exhibit local collapse. However, the connected fracture mode mostly occurs in the specimens with high porosity, and usually shows connected fracture in one or more pore layers. Moreover, the local pores of two deformation modes present different characteristics during compression, and the stress concentration occurs at the position with the minimum curvature of the pores. Microstructural analysis indicates that shear band appearing in the intercellular walls is the main failure mechanism of the specimens. Dimples and ductile stripes of fracture surface reveal that the collapse of the intercellular wall is a process of ductile fracture. Meanwhile, the softening failure of the cell walls and the strain hardening of the matrix material can affect the mechanical response of porous titanium. Additionally, with the increase of porosity, the greater the stress concentration factor, the easier the failure of porous metals.

Key words: porous titanium; local pore; compression deformation; failure mechanism; stress concentration

Lotus-type porous metals are used as integrated structure-function engineering materials[1-4], which have received widespread attention. Their practical applications include many fields such as lightweight structures, and aerospace or automotive engineering[5,6]. This is mainly attributed to their low density, excellent energy absorption capacity and thermal conductivity[7,8].

Lotus-type porous metals with long cylindrical pores can be fabricated by unidirectional solidification technique[9,10]. In recent years, many lotus-type porous metals have been successfully prepared and extensively studied. These studies mainly focus on the effect of porosity, loading rate, heat treatment, loading direction and pore topology on the mechanical properties of porous metals. For example, Wang et al[11] fabricated the regular lotus-type porous titanium and investigated their mechanical properties. The results showed that yield strength increases with increasing the strain rate and decreases with increasing the porosity. Ren et al[12] studied the mechanical response of high-speed impact on porous titanium using one-stage gas gun plate impact technique, and the results indicated that the peak pressure is reduced due to the influence of voids in the process of wave propagation. Yang et al[13] fabricated the porous TiAl-Nb alloys, and compared the mechanical properties in the loading direction parallel and perpendicular to the pore direction. The results indicated that the specimens exhibit superior compressive properties, when the loading direction is parallel to the direction of the pores. Matej et al[14] investigated the effect of pore topology on mechanical properties, and found that simplified porous model with $\pi/4$ rotated aligned regular pores gives a very good approximation to the material behavior.

Additionally, numerous studies have also shown that deformation failure of porous metals is closely related to mechanical properties and energy absorption. For instance, Song et al[15] fabricated porous S30C and S45C carbon steels with unidirectional cylindrical pores, and found that there is

Received date: October 25, 2020
Foundation item: National Natural Science Foundation of China (11872124)
Corresponding author: Ning Jianguo, Ph.D., Professor, State Key Laboratory of Explosion Science and Technology, Beijing Institute of Technology, Beijing 100081, P. R. China, Tel: 0086-10-68914561, E-mail: jgning@bit.edu.cn

no plateau stress stage. The main reason is that localized deformation and crack formation promote densification in the early stage of the stress-strain curve during compression perpendicular to the pore orientation. However, compression parallel to the direction of the pores produces a plateau stress region, because rapid crack propagation is suppressed by the ductility of the matrix and formation of deformation bands. Li et al[16,17] prepared the lotus-type porous copper using a customized unidirectional solidification apparatus, and the results showed that the energy absorption process is predominantly mediated by buckling of cell walls in the direction parallel to the longitudinal pore axes, while the energy absorption capacity is mainly dissipated as plastic working through gradual squeeze, collapse and closure of pores as the loading direction is perpendicular to the pore extension direction. Tane et al[18] investigated the porous iron with dynamic compression parallel to its cylindrical unidirectional pores at 298 and 77 K, and obtained that the macroscopic deformation bands reduce the work hardening rate of plateau stress.

However, researchers cannot precisely control the morphology and topology of pores through the used techniques for fabricating lotus-type porous metals[19]. Thus, previous works mainly focus on the compressive behavior of whole porous specimens and ignore the deformation characteristics of local pores. In fact, the sum of the plastic work of all cells is the energy absorption of the whole specimen. Meanwhile, the load-bearing capacity of all cells is the ability of the whole specimen to resist external loading during the compression of the porous metals. Therefore, it is necessary to investigate the compressive behavior of the local pores, which is rarely reported in previous works.

Regular lotus-type porous specimen has homogeneous microstructure distribution. They show relatively uniform deformation characteristics during the compression, which is conducive to understand the compressive behavior of local pores. In this work, a series of regular porous titanium specimens with different porosities were fabricated to highlight the deformation characteristics of the pores during the compression of the specimens. Dynamic compression experiments and numerical simulations were implemented to analyze the compressive behavior. Meanwhile, stress concentration of the pores and failure mechanism of intercellular walls were also investigated. Based on this work, it is expected to understand the deformation failure of porous metals from the perspective of the pores.

1 Experiment

1.1 Specimen preparation

In this work, commercial pure titanium TA2 was used as the matrix material. Three groups of regular porous titanium specimens with different porosities of 20%, 33% and 45% were fabricated by mechanical drilling technique, named as P20, P33 and P45 according to the porosity, respectively. Herein, each pore layer has uniformly distributed cylindrical pores, and the pore axis between adjacent pore layers is orthogonally distributed, as shown in Fig. 1. Meanwhile, the detailed geometric parameters of the specimens are listed in Table 1.

1.2 Dynamic compression tests

The dynamic compression tests were conducted using split Hopkinson pressure bar (SHPB) system, which is commonly used to investigate the compressive behavior of solid material with strain rate ranging from 10^2 s^{-1} to 10^4 s^{-1}. Currently, the experimental apparatus, as shown in Fig.2, is employed to test the mechanical properties of porous materials[13,14]. The principle of the apparatus can be simply described as follows. When the projectile is launched onto the free end of the input bar, an incident wave, which is shaped by a reshaper, is generated and propagated toward the other end of the test system. As the wave reaches the end face of specimen, part of stress pulse is reflected back to input bar to form a reflected wave, and part of the pulse is transmitted to the output bar to form a transmitted wave. The incident wave ε_I and reflected wave ε_R are recorded by the strain gage located in the middle of the input bar, and the transmitted wave ε_T is captured by strain gage of the output bar. Finally, these data are stored in PC through the dynamic strain indicator. The stress σ, strain ε and strain rate $\dot{\varepsilon}$ are obtained by wave propagation theory[20].

$$\sigma = \frac{E_b A_b}{2A_s}(\varepsilon_I + \varepsilon_R + \varepsilon_T) \quad (1)$$

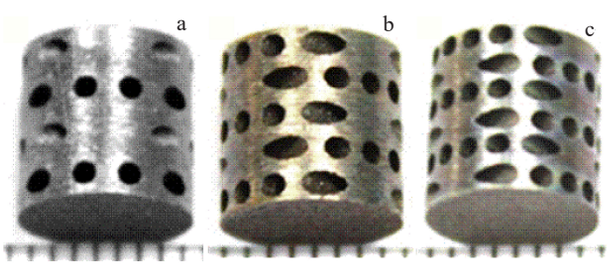

Fig.1 Images of the specimens: (a) P20, (b) P33 and (c) P45

Table 1 Geometric parameters of the regular porous titanium specimen

Specimen	Number of pore layer	Porosity/%	Diameter of specimen/mm	Height of specimen/mm	Diameter of pore/mm	Distance between two adjacent pore centers/mm	Distance between two adjacent pore layers/mm
P20	4	20	8.0	8.0	1.0	2.00	2.00
P33	5	33	8.0	8.0	1.0	1.60	1.60
P45	6	45	8.0	8.0	1.0	1.33	1..33

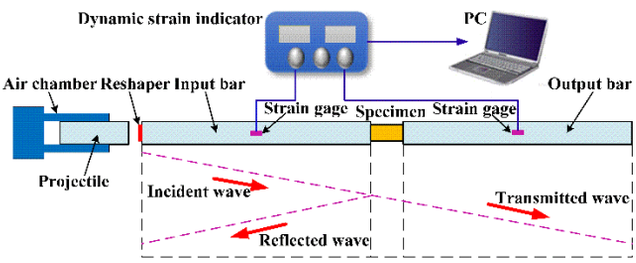

Fig.2 Schematic of split Hopkinson pressure bar

$$\varepsilon = \frac{c_b}{l_s}\int_0^t (\varepsilon_I - \varepsilon_R - \varepsilon_T)\mathrm{d}t \quad (2)$$

$$\dot{\varepsilon} = \frac{c_b}{l_s}(\varepsilon_I - \varepsilon_R - \varepsilon_T) \quad (3)$$

where E_b is the elastic modulus of the bar; A_b and A_s are the cross-sectional areas of the bar and the specimen, respectively; c_b is the elastic wave speed of bar; l_s is the length of the specimen.

A steel system with 14.5 mm diameter bars was used to investigate the mechanical properties of the specimens at the of strain rates ranging from 600 s^{-1} to 2100 s^{-1}. The length of the projectile was 200 mm, while the input and output bars were 1000 mm. In addition, grease was smeared on both ends of the specimen to minimize the friction under impact loading.

2 Numerical Simulation

2.1 Specimen and pore layer model

Specimen P20 was selected as a representative, as shown in Fig. 3a. Three-dimensional geometric model of specimen P20 is cut along the middle plane, and the sectional view is displayed in Fig. 3b. The plane model of pore layer exhibited in Fig.3c is extracted from the sectional view of P20 specimen to reveal the deformation process of pores. Afterwards, the geometric parameters of the pore layer for different specimens are listed in Table 2.

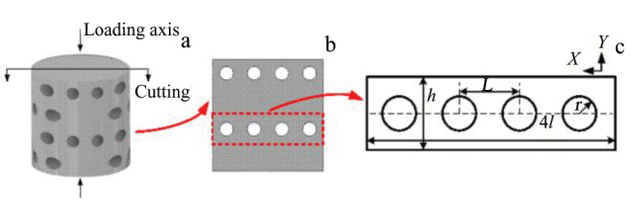

Fig.3 Specimen (a), sectional view (b) and pore layer model (c) of P20

Table 2 Geometric sizes of pore layer model for different specimens

Specimen	*L*/mm	*h*/mm	*r*/mm
P20	2.00	2.00	0.50
P33	1.60	1.60	0.50
P45	1.33	1.33	0.50

2.2 Finite element analysis

Commercial software LS-DYNA was used to simulate the three-dimensional geometric models of specimens and the two-dimensional plane models of pore layers for three groups of specimens. Solid element and shell element were applied to three-dimensional and two-dimensional models, respectively. A moving rigid wall was placed on one side of the model, and a fixed rigid wall was added to the other side. The loading velocity of the moving rigid wall was defined by $v=\dot{\varepsilon}h$, where $\dot{\varepsilon}$ is experimental strain rate, and h is the height of the model. For example, in this work, when the strain rate of specimen P20 is 2100 s^{-1}, the loading velocity v of the specimen model is 16.8 m/s (h=8 mm), while the corresponding pore layer model is loaded at a speed of 4.2 m/s (h=2 mm). Similar loading setting was also applied in previous work[21]. Additionally, the nominal stress and nominal strain can be calculated by $\sigma=F/A$ and $\varepsilon=\dot{\varepsilon}h$, respectively, where F is the interaction force between the model and the fixed rigid wall, A is the original surface area for the specimen model (A is $4L$ for pore layer model), and t is loading time.

Johnson-Cook strength and damage model (JC model) was employed to describe the mechanical behavior of TA2 material subjected to dynamic loading[22]. The Johnson-Cook strength model is expressed as:

$$\sigma = [A + B(\varepsilon_p)^n][1 + C\ln(\frac{\dot{\varepsilon}^p}{\dot{\varepsilon}_0^p})][1 - (\frac{T - T_0}{T_m - T_0})^m] \quad (4)$$

where σ respects the Mises flow stress, ε_p is the accumulated equivalent plastic strain, $\dot{\varepsilon}^p$ denotes the normalized equivalent plastic strain rate, $\dot{\varepsilon}_0^p$ means reference strain rate, T_0 and T_m are room temperature (299 K) and melting temperature (1933 K), respectively.

Meanwhile, the Johnson-Cook damage model was defined to simulate failure behavior. The damage model is defined as

$$\varepsilon_d = (D_1 + D_2\exp(D_3\sigma^*)[1 + D_4\ln(\dot{\varepsilon}^*)][1 + D_5T] \quad (5)$$

where the constant values of D_1, D_2, and D_3 are damage parameters related to the relationships between failure strain and stress triaxiality σ^*; D_4 and D_5 are the parameters depending on strain rate and temperature, respectively. The initial guess for the TA2 material parameters is obtained in this work[23], and then appropriate adjustment of these material constants were made until the simulation results closely matched the experimental data. The final parameters of JC model are listed in Table 3.

3 Results and Discussion

3.1 Mechanical behavior

Fig. 4 shows the compressive curves and deformed specimens at different strain rates. It is well known that the compressive stress-strain curve of porous materials exhibits

Table 3 Material parameters of JC model[24]

A/MPa	*B*/MPa	*C*	*m*	*n*	D_1	D_2	D_3	D_4	D_5
610	510	0.029	0.72	0.6	0.09	0.27	0.48	0.014	3.87

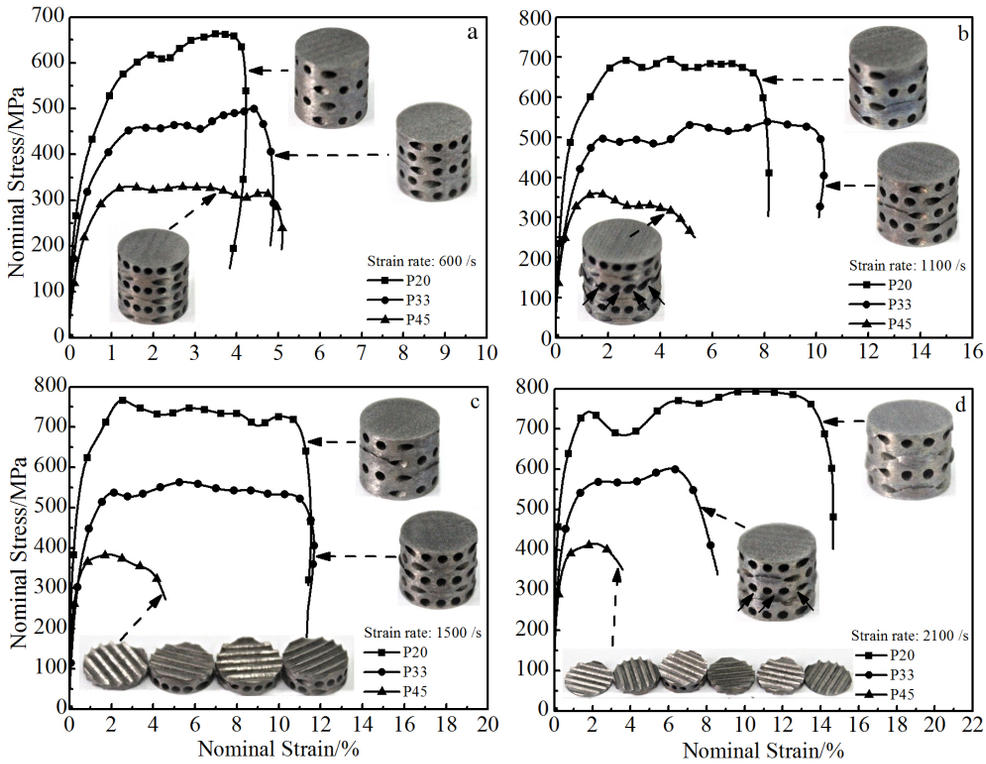

Fig.4 Compressive curves of deformed specimens at various strain rates: (a) 600 s^{-1}, (b) 1100 s^{-1}, (c) 1500 s^{-1} and (d) 2100 s^{-1}

three-stage characteristics including linear-elastic stage, plateau stage and densification stage[3,10,13]. The curves first undergo a linear-elastic stage where stress increases linearly with strain, and then slowly increase and gradually enter the plateau stage. Afterwards, the curves present a significant stress drop, which is different from the rapid rise during the densification stage. Similar curve characteristics also appear in other porous materials[21]. As expected, the compressive strength of the specimens decreases with increasing the porosity. However, it is worth noting from Fig. 4a that specimen P20 with strain rate of 600 s^{-1} has significant strain hardening in plateau region, but the degree of strain hardening gradually decreases as the porosity increases. It is due to the mutual coupling between the strain hardening of matrix material and the softening failure of cell walls during compression. For example, specimen P20 with low porosity exhibits strain hardening in plateau region due to strain rate effect of the matrix material TA2[24]. Specimen P45 with high porosity is prone to cause softening failure of cell wall, resulting in limited strain hardening, as shown in Fig. 4a. Moreover, through the comparison of the compressive curves in Fig.4a and Fig.4c, it can be seen that the plateau stress of specimen P20 presents a trend of reduction as strain rate increases. This means that the softening failure of cell walls is more significant when strain rate is higher. Similarly, other compressive curves in Fig. 4a~4c also reveal the coupling effect (strain hardening and softening failure) on the plateau stress. Meanwhile, it needs to be pointed out that the plateau stress in Fig.4d has relatively serious fluctuations owing to the high loading strain rate, so the coupling effect is not obvious in this work.

Additionally, the deformed specimens subjected to different strain rates are also shown in Fig. 4. Deformation mode was investigated by the characteristics of the deformed specimens. In Fig. 4a, cracks gradually appear on outer surface of the specimen during compression, and the collapse regions of the specimen are more serious when the strain rate increases. In this case, specimen and pores only undergo compression deformation, which can be considered as compression deformation mode. However, for specimen P45, a connected fracture is presented in one pore layer at the strain rate of 1100 s^{-1}, which is marked by black arrows in Fig. 4b. When the strain rate exceeds 1100 s^{-1}, multi-layer fractures are displayed. The specimen is completely collapsed in the pore layer, which can be determined as connected fracture mode. Similarly, Vesenjak et al[25] investigated the compressive properties of a regular open-cell structure, and found that the deformation characteristics also exhibit the connected fracture mode. The deformation characteristic of specimen P30 shows compression deformation mode ($\dot{\varepsilon} < 2100\ s^{-1}$) and connected fracture mode ($\dot{\varepsilon} \geqslant 2100\ s^{-1}$).

3.2 Deformation evolution

It can be known that the deformed specimen P20 at the strain rate of 2105 s^{-1} and the specimen P45 at the strain rate of 1091 s^{-1} present two typical deformation modes, which are compression deformation mode and connected fracture mode, respectively. Thus, the stress-strain curves of specimen P20 and P45 obtained by experimental tests and numerical simulation are compared in Fig.5 at the strain rate of 1100 and 2100 s^{-1}, respectively. It can be found that the simulated

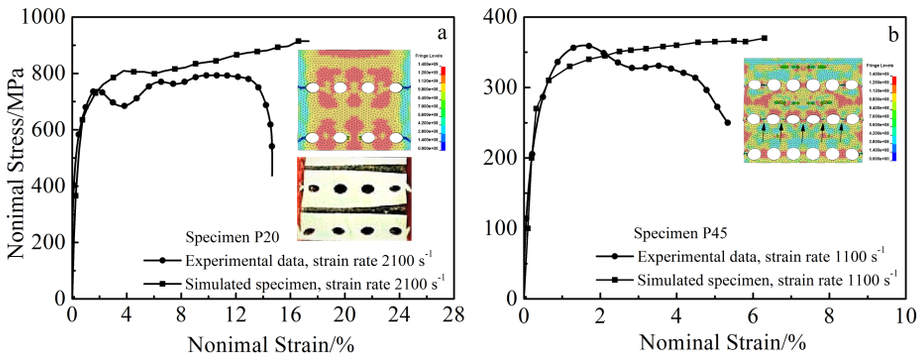

Fig.5 Comparison of experiment and simulation results for specimens P20 (a) and P45 (b)

compressive stress is close to the experimental results. Meanwhile, the cross-section of simulated specimen P20, which is sliced from the mid-plane of the specimen, is similar to the cross-sectional photograph of the deformed specimen, as shown in Fig. 5a. Fig. 5b shows that intercellular walls are collapsed in certain pore layer, which is consistent with the connected fracture mode. Comparing the curves and the simulated contour of specimens, it can be found that the experimental and simulation results are in good agreement. Thus, simulation results are considered to be able to make reliable predictions.

To understand the evolution process of two deformation modes, the evolution process of the compression deformation mode (specimen P20 with strain rate of 2100 s^{-1} is selected as representative) is exhibited in Fig. 6. It can be found in Fig. 6a that cell walls of the outer surface gradually collapse, while no serious damage appears inside the specimen. In parallel, pore layer model exhibits the deformation characteristics of the pore section, as shown in Fig. 6b. The circular pore section gradually changes to ellipse shape, and stress concentration is obvious at the minimum curvature of the pores[26]. The region of stress concentration (red region) presents compressive stress, and the upper and lower edge regions of the pores (blue region) experience tensile stress, which is similar to single pore stress distribution in infinite elastic medium[27]. Additionally, intercellular walls of the pore layer have no crack and only present plastic compression deformation.

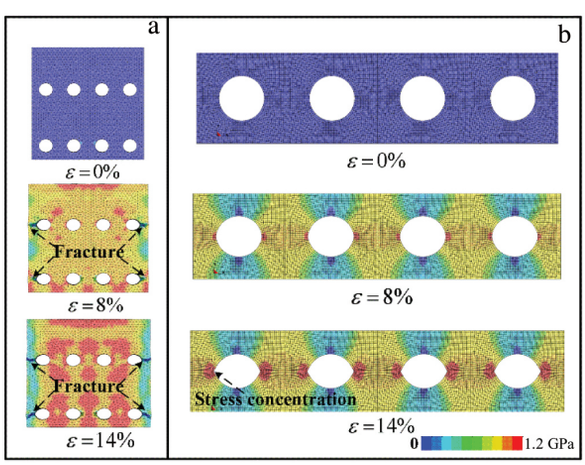

Fig.6 Stress cloud images of compression deformation of specimen P20: (a) cross-sectional images and (b) pore layer model

Fig. 7 exhibits the deformation process of the connected fracture mode (such as deformation characteristics of specimen P45 at the strain rate of 1100 s^{-1}). With gradually increasing the compressive strain, the intercellular walls of the specimen start to fracture at strain of 6% until the pore layer is completely collapsed at strain of 8%, as shown in Fig. 7a. The stress distribution of the pore layer model with different compressive strains is displayed in Fig. 7b. As compressive strain continues to increase, the intercellular walls inside the pore layer gradually start to incline and bend. Meanwhile, shape of the pore section changes from a circle to an ellipse or even a leaf shape. At the strain of 22%, the positions of the minimum curvature for the pore section gradually present cracks, which is accompanied by obvious stress concentration. It should be pointed out that the compressive deformation with the connected fracture mode is non-uniform when pore layer begins to collapse. In particular, the compressive strain of the fracture layer is larger than that of other pore layers during dynamic compression. Thus, failure strain (ε = 22%) of the pore layer model is greater than that (ε = 8%) of the specimens.

3.3 Stress concentration

Based on previous reports[10,15], collapse failure of cell walls for porous metals is mainly caused by stress concentration near the pores. Thus, stress concentration factor is introduced in this work to investigate the stress characteristics around the pores. In fact, the porosity of regular porous titanium can be determined by the distance (L) between adjacent pores and the height (h) of pore layers. Herein, the stress concentration factor K is defined as the ratio of the peak stress σ_{max} in the body to nominal stress σ, which is expressed as

$$K = \sigma_{max} / \sigma \quad (6)$$

The pore layer models of different specimens can be simplified, as shown in Fig. 8. σ is the loading nominal stress, and d, L and h are consistent with those in Fig. 3c. It is easy to find that peak stress σ_{max} appears at point A.

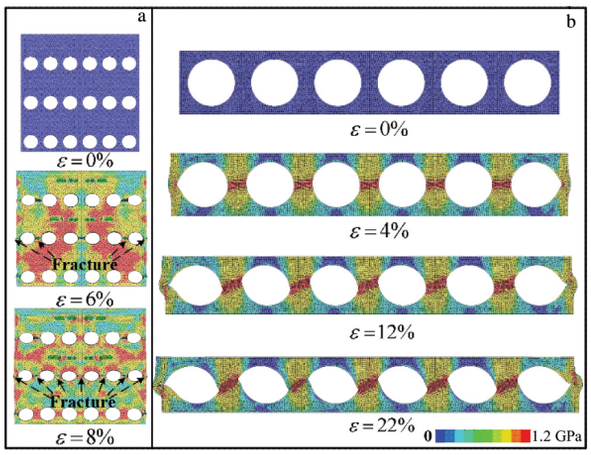

Fig.7 Stress cloud images of deformation evolution of specimen P45: (a) cross-section image and (b) pore layer model

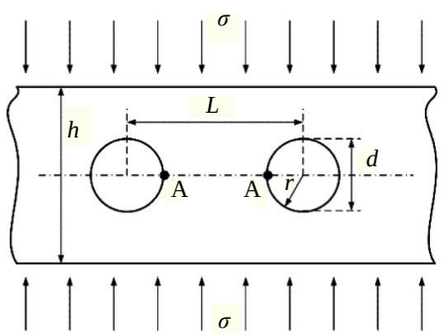

Fig.8 Schematic diagram of circular pores with equal diameter align on a line perpendicular to the loading direction

It can be known that the influence of distance between adjacent pores on stress concentrations is weak for an infinite thin element, where L is greater than $3d$. In this case, the stress concentration factor is consistent with the results of a single pore with K=3. In order to highlight the effect of pore layer height on stress concentration factors, it is assumed that the distance between adjacent pores is far enough to ignore the interaction between pores. An empirical formula is concluded by Peterson[28] to cover d/h range.

$$K = 2 + (1 - \frac{d}{h})^3 \qquad (L > 3d) \qquad (7)$$

In parallel, considering the effect of distance between adjacent pores on stress concentration factors (here $h \to \infty$), a conclusion based on mathematical analyses is summarized as

$$K = 3 - 3.095(\frac{d}{L}) + 0.309(\frac{d}{L})^2 + 0.785(\frac{d}{L})^3 \qquad (8)$$

Fig. 9 shows that Eq. (7) and Eq. (8) exhibit the variation characteristic of the stress concentration factor in the infinite plane model. It can be found that the stress concentration factor decreases monotonically with increasing d/h or d/L in Eq. (7) and Eq. (8). When h and L are infinity, the stress concentration factor is close to 3. With h and L approaching d, the stress concentration factors are close to 2 and 1,

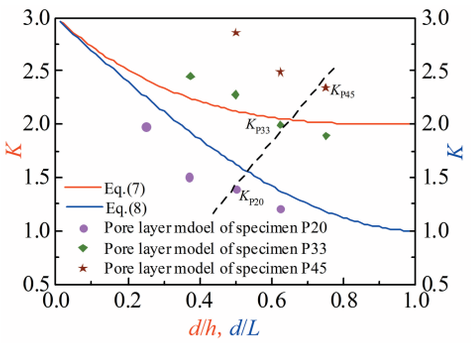

Fig.9 Variation of stress concentration factor with d/h or d/L

respectively. It clearly reveals that boundary conditions have obviously influence on the stress concentration factors. However, there is a strong influence between the pores of the porous metal due to the close distance. Therefore, it is very difficult to establish a theory model to accurately describe the effect of diameter d, height h and distance L on stress concentration factor K. Herein, based on the pore layer model, numerical simulation is used to carry out a series of parameter studies, where diameter d is constant, h corresponds to the height of the pore layer model for different specimens, and distance L is changed. The results show that stress concentration factor K exhibits a decreasing trend as the distance L decreases. Meanwhile, the stress concentration factors (K_{P20}, K_{P33} and K_{P45}) of pore layer models for specimen P20, P33 and P45 are also compared, and they present an increasing trend with increasing the porosities. Actually, this also reveals a fact that with the increase of porosity, the greater the stress concentration factor, the easier the failure of porous metals.

3.4 Failure mechanism

To reveal the failure mechanism of intercellular walls under dynamic loading, polishing of intercellular walls was completed using a polishing machine. Polished regions were cleaned with distilled water and etched with Kroll's reagent. Thereafter, microstructure analysis was completed by scanning electron microscope (SEM, S-4800). The initial circular pore in Fig. 10a gradually transforms into leaf shape, as shown in Fig. 10b, and the initial cracks are generated at the minimum curvature of pores. It can be known from Fig. 10c that crack of adjacent pores begins to extend and converge in opposite directions. Actually, these reveal that the failure of regular porous titanium is associated with the fracture of intercellular walls. When the specimen is impacted under high strain rate, the cracks appear in the stress concentration region of the pores. Meanwhile, the front of the crack shows localized plastic deformation zone, which is formed within the shear plane in the direction of the shear stress. The localized plastic deformation zone is regarded as the shear band[29]. As magnified and observed at multiples, the distinct shear band can be observed in the intercellular wall, as shown in Fig. 10d~10f. When the specimen is impacted, the temperature in the shear band rapidly approaches the melting point, and material

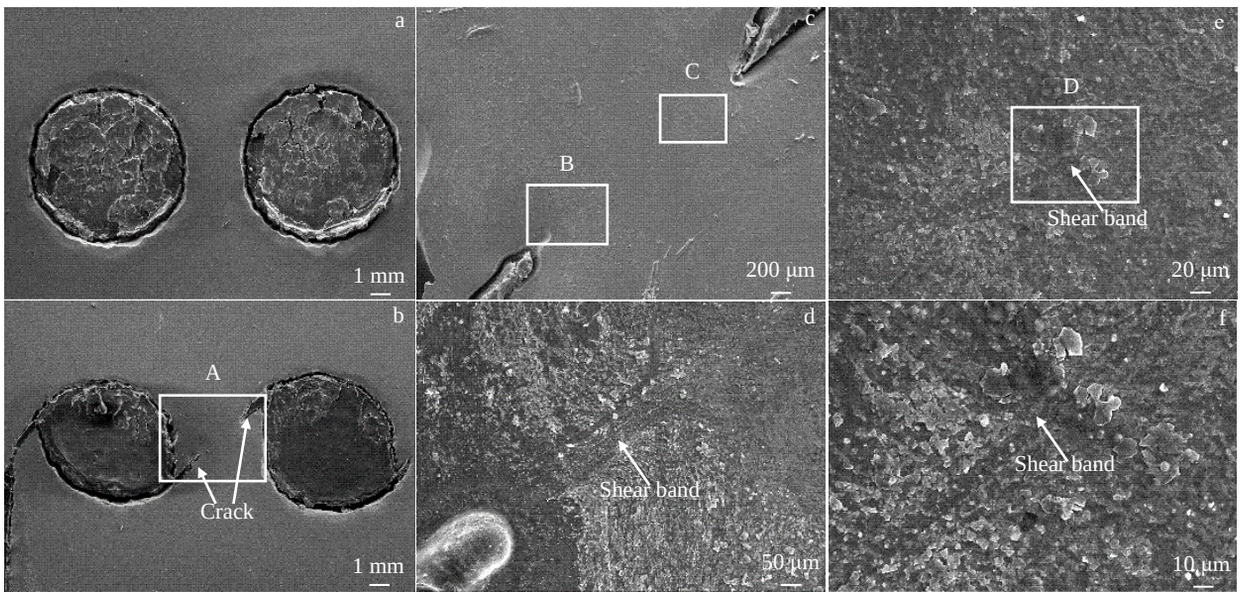

Fig.10 Shear band observed in the intercellular wall: (a) initial pores, (b) deformation pores, (c) larger view of section A, (d) B area enlargement, (e) larger view of section C and (f) D area enlargement

tends to flow within the shear band. For higher strain rates, shear band forms more easily because higher temperatures can be reached for a certain plastic deformation with less heat dissipation. As a result, shear fracture of the regular porous titanium occurs in the intercellular walls, and the shear band is the main failure mechanism. In fact, the process is also the main reason for softening failure in the plateau stage of the stress-strain curves.

For insight into the characteristics of fracture surface, specimens were cleaned with ultrasonic cleaner where distilled water was used as the cleaning solvent. Then micrographs of fracture surface for the specimen P45 with strain rate 1091 s^{-1} were observed using SEM, which are displayed in Fig.11. Fig.11a shows the morphology taken at an angle perpendicular to the fracture surface. The larger view of section A shows that the fracture surface of cell walls is a

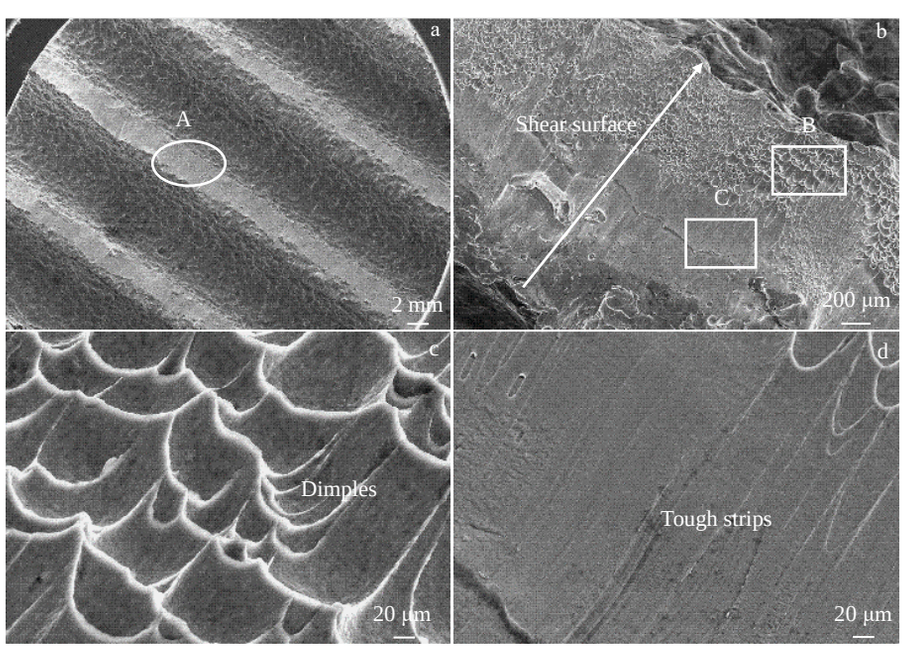

Fig.11 Morphologies of fracture surface for specimen P45 at strain rate of 1091 s^{-1}: (a) fracture surface, (b) larger view of section A, (c) B area enlargement and (d) larger view of section C

sloping shear surface, as shown in Fig.11b. It can be observed that a large amount of dimples with parabolic patterns appear on the failure surface, as shown in Fig.11c. These dimples are formed due to the growth and convergence of adjacent micro-voids. In the process, the dimples are stretched severely and they take the shape of parabolic patterns under shear stress[30]. Meanwhile, tough strips (Fig. 11d) are also presented along with the shear surface[31,32], which are caused by the rapid expansion of cracks. In fact, crack propagation is relatively slow at the initial stage, and the corresponding fracture surface is stretched to produce the dimples. Subsequently, rapid propagation of cracks causes the tough strips on the fracture surface. Based on the above analyses, it can be concluded that the failure mechanism is the shear band of intercellular walls. Stretched dimples and tough strips generally form on the fracture surface. The collapse failure of intercellular walls is a process of ductile fracture.

4 Conclusions

1) Porous titanium specimens with different porosities exhibit two typical deformation modes: compression deformation mode and connected fracture mode. Generally, the compression deformation mode mainly occurs in the specimens with low porosity, and the failure characteristics are that the cell walls of outer surface of the specimen exhibit local collapse. The connected fracture mode mostly appears in the specimen with high porosity, and usually shows connected fracture in one or more pore layers.

2) The local pores of two deformation modes present different characteristics during compression, and the stress concentration occurs in the position with minimum curvature of the pores. For the connected fracture mode, the initial cracks of intercellular walls are generated at the stress concentration region.

3) Shear band appearing in the intercellular walls is the main failure mechanism of the specimen. Dimples and ductile stripes of fracture surface reveal that the collapse of the intercellular walls is a process of ductile fracture. Meanwhile, the softening failure of the cell walls and the strain hardening of the matrix material can affect the mechanical response of the porous titanium during dynamic compression.

4) With the increase of the porosity, the greater the stress concentration factor, the easier the failure of porous metals.

References

1 Nakajima, Hideo. *Proceedings of the Japan Academy, Series B* [J], 2010, 86(9): 884

2 Tan Ping, Tang Huiping, Wang Jianyong *et al*. *Rare Metal Materials and Engineering*[J], 2006, 35(S1): 433

3 Zang Chunyong, Tang Huiping, Wang Jianyong. *Rare Metal Materials and Engineering*[J], 2009, 38(S1): 437

4 Nakajima, Hideo. *Materials Science Forum*[J], 2010, 654-656: 1452

5 Zhao B, Gain A K, Ding W *et al*. *The International Journal of Advanced Manufacturing Technology*[J], 2018, 95: 2641

6 Liu P S, Li T F, Fu C. *Journal of Functional Materials*[J], 2001, 32(1): 12

7 Yuan L, Huawei Z, Xiang C *et al*. *China Foundry*[J], 2005, 2(3): 184

8 Nakajima H, Hyun S K, Park J S *et al*. *Materials Science Forum* [J], 2007, 539-543: 187

9 Zhou Canxu, Liu Yuan, Zhang Huawei *et al. Transactions of Nonferrous Metals Society of China*[J], 2020, 30(6): 1524

10 Nakajima Hideo, Ide Takuya. *Materials Science Forum*[J], 2018, 933: 49

11 Wang Jin, Ren Huilan, Shen Haiting *et al*. *Chinese Journal of High Pressure Physics*[J], 2017, 31: 364

12 Ren Huilan, Wang Jing, Hao Li *et al*. *Science China Technological Sciences*[J], 2017(4): 1

13 Yang F, Tane M, Lin J P *et al*. *Materials & Design*[J], 2013, 49: 755

14 Matej Vesenjak, Massakazu Tane, Matej Borovinsek *et al*. *Computational Materials Science*[J], 2012, 65: 37

15 Song Y H, Tane M, Nakajima H. *Materials Science & Engineering A*[J], 2012, 534: 504

16 Li Weidong, Xu Kai, Li Honghao *et al. Journal of Materials Science & Technology*[J], 2017, 33: 1353

17 Li Weidong, Jia Haoling, Pu Chao *et al. Journal of Materials Science & Technology*[J], 2015, 31(10): 1018

18 Tane M, Zhao F, Song Y H *et al*. *Materials Science & Engineering A*[J], 2014, 591(3): 150

19 Körner C, Singer R F. *Advanced Engineering Materials*[J], 2010, 2(4): 159

20 Gray G T. *ASM Handbook*[S]. Ohio: ASM International, Materials Park, 2000: 462

21 Xiao L, Song W, Wang C *et al*. *International Journal of Impact Engineering*[J], 2017, 100: 75

22 Biswas N, Ding J L. *International Journal of Impact Engineering* [J], 2014, 82: 89

23 Fu Yingqian. *Initiation and Propagation of Adiabatic Shear Localization*[D]. Ningbo: Ningbo Univeristy, 2013

24 Peng J, Zhou C, Dai Q *et al*. *Rare Metal Materials and Engineering*[J], 2013, 42(3): 483

25 Vesenjak M, Ren Z, Chsner A. *Material Wissenschaft und Werkstofftechnik*[J], 2008, 39(2):125

26 Tomá Oplt, Hutar P, Pokorny P *et al*. *International Journal of Fatigue*[J], 2019, 118: 249

27 Badiger S, Ramakrishna D S. *Advances in Structures, Systems and Materials*[M]. Ramaiah: Ramaiah University of Applied Sciences, 2020

28 Peterson, Rudolph Earl, Pilkey *et al*. *Peterson's Stress Concentration Factors*[M]. Wiley, 2007, 34(2)

29 Timothy S P, Hutchings I M. *Fatigue & Fracture of Engineering Materials & Structures*[J], 2010, 7(3): 223

30 Xu Zejian, He Xiaodong, Hu Hongzhi *et al*. *International*

Journal of Impact Engineering[J], 2019, 130: 281

31 Meyers M A, Chen Y J, Marquis F D S *et al*. *Metallurgical and Materials Transactions A*[J], 1995, 26(10): 2493

32 Xie J, Shi Y W. *Energy Policy*[J], 2013, 32(32): 1033

不同孔隙率规则多孔钛的变形失效特征

任会兰，申海艇，宁建国

(北京理工大学 爆炸科学与技术国家重点实验室，北京 100081)

摘　要：设计和制备了孔隙率不同的3组规则多孔钛试样，采用分离式霍普金森压杆实验装置，开展了应变率范围在600~2100 s^{-1}的单轴压缩实验，研究了加载过程中整个试样和局部孔洞的变形失效特征。结果表明，试样展示出2种典型的变形模式：压缩变形模式和连通断裂模式。压缩变形模式主要发生在低孔隙率的试样，试样的外表面胞壁出现局部塌陷，而连通断裂模式易发生在高孔隙率的试样中，常在试样的一个或多个孔层出现连通的断裂。另外，2种变形模式下的局部孔洞也呈现出不同的形状变化特征，且在孔洞最小曲率的位置都形成明显的应力集中，相应的应力集中因子随试样孔隙率的增大而增大。微结构分析显示：剪切带是试样失效的主要机制，试样的断口容易产生韧窝和韧性条纹。

关键词：多孔钛；局部孔洞；压缩变形；失效机制；应力集中

作者简介：任会兰，女，1973年生，博士，教授，北京理工大学爆炸科学与技术国家重点实验室，北京 100081，电话：010-68918315，E-mail：huilanren@bit.edu.cn